Progress In Electromagnetics Research, Vol. 134, 23–46, 2013

AN IMPROVED SCHEME FOR PARAMETER ESTIMATION OF G^0 DISTRIBUTION MODEL IN HIGH-RESOLUTION SAR IMAGES

Jianghua Cheng*, Gui Gao, Wenxia Ding, Xishu Ku, and Jixiang Sun

College of Electronic Science and Engineering, National University of Defense Technology, Changsha, Hunan 410073, P. R. China

Abstract—Statistical modeling of Synthetic Aperture Radar (SAR) images is of great importance for speckle noise filtering, target detection and classification, etc. Moreover, it can provide a comprehensive understanding of terrain electromagnetics scattering mechanism. Over the past three decades, many sophisticated models have been developed for SAR images, such as Rayleigh, Gamma, K and G etc. The G^0 distribution is a special form of the G model, which can model the speckle fluctuations of many classes of objects like homogeneous, heterogeneous and extremely heterogeneous ones, and is widely used in SAR images interpretation. However, as many improvements have been performed on SAR sensors, the traditional parameter estimation methods of the G^0 distribution may be not sufficient, notably in high resolution SAR images. They cannot arrive at a solution frequently when modeling regions in high resolution SAR images, especially the extremely homogeneous regions. In order to deal with this problem, this paper proposes an improved parameter estimation scheme of the G^0 distribution, which combines the classical moment estimation with the mellin transform. To quantitatively assess the fitting precision of the proposed method, we adopt the Kullback-Leibler (KL) distance, Kolmogorov-Smirnov (KS) test and Mean Square Error (MSE) as similarity measurements. The advantage of this proposed parameter estimation method becomes evident through the analysis of a variety of areas (ground vegetation, trees and buildings) in two high resolution SAR images.

Received 23 August 2012, Accepted 9 November 2012, Scheduled 14 November 2012

* Corresponding author: Jianghua Cheng (jianghua_cheng@nudt.edu.cn).

1. INTRODUCTION

With the development of remote sensing technique, earth observation and environmental monitoring [1] have been known a considerable boom in various applications. SAR [2] is one of the most important active sensors for earth observation and environmental monitoring, can detect electromagnetic radiation emitted or reflected by objects, and plays an important role in detecting [3, 4] and discriminating targets [5–7]. The advantage of SAR compared with other positive sensors lies in its capability of imaging weather and illumination independent. The precise knowledge of the statistical properties of SAR data and backscattering model [8–15] plays a central role in SAR image processing and understanding [16]. Therefore, statistical modeling of SAR images has become an active research field and numbers of well-known statistical models have been proposed over the past three decades.

The existing statistical models of SAR images are customarily divided into two categories: nonparametric and parametric models [17]. There exist several representative nonparametric models, such as the artificial neural networks (ANN) [18–22], the support vector machine (SVM) [23, 24], the parzen window [25], etc. The essentially part of these nonparametric models is using the weighted sum of different kernel functions to approximate the statistical distribution of SAR images. The merit of nonparametric modeling is suitable for estimating the complex unknown probability density function (PDF) and has relatively high estimation accuracy. However, it needs a mass of sample data set as well as involves complex computation. Consequently, parametric modeling has been intensively studied. The underlying idea of parametric modeling is choosing an appropriate statistical model from several given ones to approximate the statistical distribution of SAR images. Currently, most widely used statistical models are developed from the product speckle model, which is based on the assumption that the observed data results from the product between the speckle noise and the terrain backscatter. Several distributions have been used for the backscatter, aiming at modeling different types of classes and their characteristic degrees of homogeneity, such as Rayleigh distribution [26] for single-look amplitude SAR images and Gamma distribution [27] for multi-look amplitude SAR images. The K distribution [28, 38] is deduced from the assumption that the intensity of radar cross section (RCS) fluctuations has a Gamma distribution in heterogeneous regions. It has multiplicative fading statistical characteristics which usually provides a good fitness to heterogeneous terrains. Therefore, the K distribution has become a well-known statistical model recently. However, the K distribution cannot model extremely heterogeneous objects in high resolution SAR images. To solve this problem, the G distribution [16] is proposed by assuming a Gamma distribution for the speckle noise and a square root of generalized inverse Gaussian (SRGIG) distribution for the terrain backscatter of multi-look SAR images. It is first presented by the G distribution that SAR image scenes can be divided into homogeneous, heterogeneous and extremely heterogeneous parts according to their homogeneous degrees. The K and G^0 distributions are just the two special forms of the G distribution [16], where the K distribution is suitable for modeling heterogeneous regions while the G^0 distribution is suitable for modeling multilook clutter with widely varying degrees of homogeneity. Compared with the G distribution, the G^0 distribution does not involve complex Bessel functions. So the parameter estimation of the G^0 distribution is relatively easy, and the computational complexity is low. Consequently, the G^0 distribution has become one of the most promising statistical models in recent years [29, 30].

The essential part of the G^0 distribution is parameter estimation. Several strategies have been proposed to deal with parameter estimation problem, such as the method of moments (MoM) [16, 29, 31–33] and mellin transform (MT) based parameter estimation [34]. However, the fitting precision of the MoM is low. The MT based method can not model extremely homogeneous regions although it has a high estimation precision.

This paper proposes a new parameter estimation method by combing use of the MoM and the MT. The structure of this paper is as follows. In Section 2, methods like the MoM, MT and our proposed are introduced. In Section 3, experimental results of parameter estimation are discussed and the KL distance KS test and MSE are used to quantitatively assess the fitting precision of the above mentioned methods. In Section 4, conclusions are reached.

2. METHODOLOGY

In order to retrieve the “unspeckled” radar backscatter component from an observed SAR image data, a model combining an underlying RCS component with an uncorrelated speckle component is used. The most commonly used model is the product model, which expresses the observed component Z as the product of the RCS component X and the speckle noise component Y

$$Z = X \cdot Y \tag{1}$$

Frery et al. [16] deduced the G model by assuming a generalized inverse Gaussian distribution for the RCS component and a Gamma distribution for the speckle component of multi-look SAR images. The intensity and amplitude PDF of the G distribution are

$$\begin{aligned} & p_{Z_I}(x) \sim G_I(\alpha, \gamma, \lambda, n) \\ & = \frac{n^n (\lambda/\gamma)^{\alpha/2}}{\Gamma(n) K_\alpha\left(2\sqrt{\lambda\gamma}\right)} x^{n-1} \left(\frac{\gamma + nx}{\lambda}\right)^{(\alpha-n)/2} K_{\alpha-n}\left(2\sqrt{\lambda\left(\gamma + nx\right)}\right) \end{aligned} \tag{2}$$

$$\begin{aligned} & p_{Z_A}(x) \sim G_A(\alpha, \gamma, \lambda, n) \\ & = \frac{2n^n (\lambda/\gamma)^{\alpha/2}}{\Gamma(n) K_\alpha\left(2\sqrt{\lambda\gamma}\right)} x^{2n-1} \left(\frac{\gamma + nx^2}{\lambda}\right)^{(\alpha-n)/2} K_{\alpha-n}\left(2\sqrt{\lambda(\gamma + nx^2)}\right) \end{aligned} \tag{3}$$

where $p_{Z_I}(x)$ is the intensity PDF, $p_{Z_A}(x)$ is the amplitude PDF, $x \in \mathbb{R}$ is the RCS component, n is the equivalent number of looks, λ, γ are the scale parameters which have a relationship with the mean energy of the observed region, K_α denotes the modified Bessel function of the third kind, α indicates the degree of heterogeneity [16], and $\Gamma(\cdot)$ denotes the Gamma function.

The K distribution is a particular form of the G model, which assumes that both the RCS component and the speckle component as Gamma distribution. If $\gamma \to 0$, the intensity and amplitude PDF of K distribution can be deduced from Equation (1), Equation (2) and Equation (3) respectively

$$\begin{aligned} & p_{Z_I}(x) \sim K_I(\alpha, \lambda, n) \\ = \; & \frac{2\lambda n}{\Gamma(\alpha)\Gamma(n)} (\lambda n x)^{(\alpha+n)/2-1} K_{\alpha-n}\left(2\sqrt{\lambda n x}\right), \quad \alpha, \lambda, n, x > 0 \end{aligned} \tag{4}$$

$$\begin{aligned} & p_{Z_A}(x) \sim K_A(\alpha, \lambda, n) \\ = \; & \frac{4\lambda n x}{\Gamma(\alpha)\Gamma(n)} (\lambda n x^2)^{(\alpha+n)/2-1} K_{\alpha-n}\left(2x\sqrt{\lambda n}\right), \quad \alpha, \lambda, n, x > 0 \end{aligned} \tag{5}$$

The Gamma distribution can describe the characteristics of the RCS fluctuations of heterogeneous terrains well in high resolution SAR images. But it cannot model extremely heterogeneous terrains like urban regions containing many buildings.

The G^0 distribution is another particular form of the G model, which assumes that the RCS component as SRGIG distribution and the speckle component as Gamma distribution. If $\lambda \to 0$, the intensity and amplitude PDF of the G^0 distribution can be deduced from Equation (1), Equation (2) and Equation (3) respectively

$$p_{Z_I}(x) \sim G_I^0(\alpha, \gamma, n) = \frac{n^n \Gamma(n-\alpha) x^{n-1}}{\gamma^\alpha \Gamma(n) \Gamma(-\alpha) (\gamma + nx)^{n-\alpha}}, \quad -\alpha, \gamma, n, x > 0 \tag{6}$$

$$p_{Z_A}(x) \sim G_A^0(\alpha,\gamma,n) = \frac{2n^n\Gamma(n-\alpha)x^{2n-1}}{\gamma^\alpha\Gamma(n)\Gamma(-\alpha)(\gamma+nx^2)^{n-\alpha}}, \quad -\alpha,\gamma,n,x>0 \quad (7)$$

The SRGIG distribution is appropriate for modeling both heterogeneous and extremely heterogeneous regions. Moreover, the PDF given in Equation (6) and Equation (7) don't involve the complex Bessel functions. Thus, it potentially means simple parameter estimation and is regarded as the universal model for speckled imagery Figure 1(a) shows some examples of Equation (7) with $n = 2$ for different values of α, and Figure 1(b) shows some examples of Equation (7) with $\alpha = -3$ for different values of n. It can be seen that parameter α is able to provide more flexibility to control the model shape than parameter n.

As mentioned in the introduction section, the existing efficient parameter estimation techniques for G^0 distribution are the MoM and MT based methods. In order to simplify the introduction, we only discuss parameter estimation for the intensity PDF of the G^0 distribution because the estimated values are same both for intensity and amplitude data.

2.1. MoM Based Parameter Estimation

The k-th order moments of the G^0 distribution are given by

$$\begin{aligned} E\left(x^k\right) &= \int_0^{+\infty} x^k G_I^0\left(\alpha,\gamma,n\right)dx \\ &= \frac{n^n\Gamma(n-\alpha)}{\gamma^\alpha\Gamma(n)\Gamma(-\alpha)}\int_0^{+\infty}\frac{x^{n+k-1}}{(\gamma+nx)^{n-\alpha}}dx, \quad -\alpha,\gamma,n,x>0 \quad (8) \end{aligned}$$

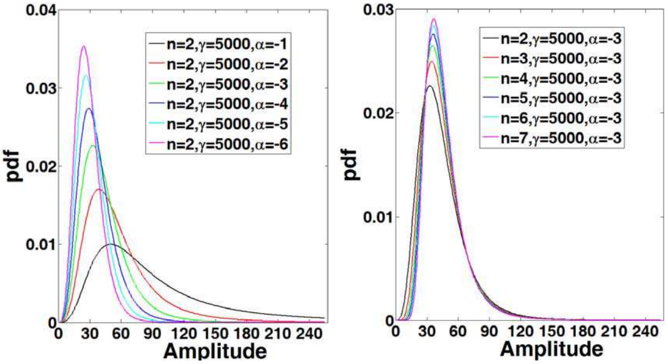

(a) (b)

Figure 1. The amplitude PDF of G^0 distribution with $\gamma = 5000$ for different values of n and α. (a) $n = 2$, $\alpha = \{-1, -2, -3, -4, -5, -6\}$. (b) $n = \{2, 3, 4, 5, 6, 7\}$, $\alpha = -3$.

After simplification, Equation (8) can be expressed as

$$E\left(x^{k}\right)=\left(\frac{\gamma}{n}\right)^{k}\frac{\Gamma(-\alpha-k)\Gamma(n+k)}{\Gamma(n)\Gamma(-\alpha)},\quad -\alpha,\gamma,n,x>0 \qquad (9)$$

In order to estimate the parameters α, γ and n, two well-known moment estimation methods exist [16, 29]. For intensity data, assuming the equivalent number of looks n known, and using $k = 1/2$, 1 [16]. The estimator for the parameters of the G^0 distribution are given

$$\begin{cases}\dfrac{\Gamma^2(-\alpha-1/2)\Gamma^2(n+1/2)}{\Gamma(-\alpha-1)\Gamma(n+1)\Gamma(-\alpha)\Gamma(n)}=\dfrac{E^2(x^{1/2})}{E(x)} \\ \gamma=n\left(\dfrac{E(x)\Gamma(-\alpha)\Gamma(n)}{\Gamma(-\alpha-1)\Gamma(n+1)}\right)^2\end{cases},\quad -\alpha,\gamma,n,x>0 \qquad (10)$$

We call this moment estimation method as the classical MoM.

Assuming the equivalent number of looks n known, and using $k = 1$, 2 [29]. The estimator for the parameters of the G^0 distribution are given

$$\begin{cases}E(x)=\dfrac{\gamma}{-(\alpha+1)} \\ E(x^2)=\dfrac{\gamma^2(n+1)}{n\alpha(\alpha+1)}\end{cases},\ \alpha<-1,\gamma,n,x>0 \qquad (11)$$

Both of these two moment estimation methods are taken the equivalent number of looks n as known. However, the equivalent number of looks of different regions varies greatly in a whole SAR image. It is reasonless to replace the mean number of looks as the number of looks of different regions, and is necessary to take n as an estimation parameter.

In order to estimate three parameters α, γ and n, three Equations are needed at least. Based on the property $\Gamma(x+1) = x\Gamma(x)$ of the gamma function $\Gamma(x) = \int_0^{\infty} t^{x-1}e^{-t}dt$ $(x > 0)$, we deduce the iterative form of moment calculation as

$$E\left(x^{k+1}\right)=-\frac{\gamma}{n}\frac{n+k}{\alpha+k+1}E\left(x^{k}\right),\quad -\alpha,\gamma,n,x>0 \qquad (12)$$

Based on Equation (12) and by using $k = 1$, 2 and 3, the estimator for the parameters of the G^0 distribution are given

$$\begin{cases}E(x)=-\dfrac{\gamma}{\alpha+1} \\ E\left(x^2\right)=\dfrac{(n+1)(a+1)}{n(a+2)}E^2(x) \\ E\left(x^3\right)=\dfrac{(n+2)(a+1)}{n(a+3)}E^2(x)E(x)\end{cases},\quad -\alpha,\gamma,n,x>0 \qquad (13)$$

We call this moment estimation method as the extended MoM.

However, both these two MoM based parameter estimation methods of the G^0 distribution mentioned above may be not sufficient to model regions in high-resolution SAR images.

2.2. MT Based Parameter Estimation

For a function f defined over $\mathbb{R}^+$ only, the integral mellin transform of f

$$\mathrm{MT}[f](x) = \int_0^{+\infty} u^{x-1} f(u) du \tag{14}$$

As the intensity PDF of a SAR image is defined over $\mathbb{R}^+$, its MT exists for all the values. It is obvious that Equation (14) has strong relations with the fourier transform. All the principal statistical moments of MT can be deduced from results of fourier transform [35]. The main functions of the G^0 distribution like First second-kind characteristic function, Second second-kind characteristic function, rth-order second-kind characteristic moment and rth-order second-kind characteristic cumulant are as follows respectively

$$\begin{aligned}\phi_I(x) = \mathrm{MT}[p_{Z_I}](x) &= \int_0^{+\infty} u^{x-1} p_{Z_I}(u) du = \int_0^{+\infty} u^{x-1} G_I^0(\alpha,\gamma,n) du \\ &= \left(\frac{\gamma}{n}\right)^{x-1} \frac{\Gamma(n+x-1)\Gamma(-\alpha-x+1)}{\Gamma(n)\Gamma(-\alpha)}, \quad \alpha < 1-x, \gamma, n, x > 0 \end{aligned} \tag{15}$$

$$\varphi_I(x) = \log(\phi_I(x)) \tag{16}$$

$$\widetilde{m_r} = \left.\frac{d^r \phi_I(x)}{dx^r}\right|_{x=1} = \int_0^{+\infty} (\log u)^r p_{Z_I}(u) du \tag{17}$$

$$\widetilde{k_r} = \left.\frac{d^r \varphi_I(x)}{dx^r}\right|_{x=1} \tag{18}$$

Combining Equation (15) and Equation (17), the first 3th-order second-kind characteristic moment can be deduced

$$\begin{cases} \widetilde{m_1} = \log(\gamma/n) + \Psi(n) - \Psi(-\alpha) \\ \widetilde{m_2} = \Psi^{(1)}(n) + \Psi^{(1)}(-\alpha) + \widetilde{m_1}^2 \\ \widetilde{m_3} = \Psi^{(2)}(n) - \Psi^{(2)}(-\alpha) + 3\left(\Psi^{(1)}(n) + \Psi^{(1)}(-\alpha)\right)\widetilde{m_1} + \widetilde{m_1}^2 \end{cases} \tag{19}$$

where $\Psi(x) = \Gamma'(x)/\Gamma(x)$ $(x > 0)$ is the digamma function, and $\Psi^{(k)}(x) = (-1)^{k+1} \int_0^\infty \frac{t^k e^{-xt}}{1-e^{-t}} dt$ is the kth-order digamma function which is also called the polygamma function. As for regular moments, the relationships between the first 3th-order second-kind characteristic moment and characteristic cumulant are [35]

$$\begin{cases} \widetilde{k_1} = \widetilde{m_1} \\ \widetilde{k_2} = \widetilde{m_2} - \widetilde{m_1}^2 \\ \widetilde{k_3} = \widetilde{m_3} - 3\widetilde{m_1}\widetilde{m_2} + 2\widetilde{m_1}^3 \end{cases} \tag{20}$$

Combining Equation (19) and Equation (20), the following Equations are obtained

$$\begin{cases} \widetilde{k_1} = \log(\gamma/n) + \Psi(n) - \Psi(-\alpha) \\ \widetilde{k_2} = \Psi^{(1)}(n) + \Psi^{(1)}(-\alpha) \\ \widetilde{k_3} = \Psi^{(2)}(n) - \Psi^{(2)}(-\alpha) \end{cases} \tag{21}$$

Define $x_1, x_2, \ldots, x_N$ as N samples of the observed data, the first 3th-order second-kind characteristic cumulant are actually calculated as

$$\begin{cases} \widetilde{k_1} = \frac{1}{N} \sum\limits_{i=1}^{N} \log(x_i) \\ \widetilde{k_2} = \frac{1}{N} \sum\limits_{i=1}^{N} \left[\left(\log(x_i) - \widetilde{k_1} \right)^2 \right] \\ \widetilde{k_3} = \frac{1}{N} \sum\limits_{i=1}^{N} \left[\left(\log(x_i) - \widetilde{k_1} \right)^3 \right] \end{cases} \tag{22}$$

The solution of Equation (21) is usually done by calculating the second and third expression firstly. Define two new functions by replacing α as x in Equation (21)

$$\begin{cases} f_1(x) = \left(\Psi^{(1)}\right)^{-1} \left(\widetilde{k_2} - \Psi^{(1)}(-x)\right) \\ f_2(x) = \left(\Psi^{(2)}\right)^{-1} \left(\widetilde{k_3} + \Psi^{(2)}(-x)\right) \end{cases}, \quad x < 0 \tag{23}$$

where $(\Psi^{(1)})^{-1}(x)$ is the inverse 1th-order digamma function, and $(\Psi^{(2)})^{-1}(x)$ is the inverse 2th-order digamma function. According to the property of the polygamma function, $\Psi^{(1)}(x)$ is completely monotonic increase while $\Psi^{(2)}(x)$ is completely monotonic decrease. Based on this fact, it is easy to see that $f_1(x)$ is completely monotonic decrease while $f_2(x)$ is completely monotonic increase. The intersection point of $f_1(x)$ and $f_2(x)$ is the estimated value of α. After calculating the parameter α, n and γ are obtained by Equation (21).

The MT based parameter estimation method can model homogeneous, heterogeneous and extremely heterogeneous regions of SAR image, and has a high estimation precision. The key point of all the merits mentioned above is based on the fact that functions

$f_1(x)$ and $f_2(x)$ should have an intersection point. However, the parameter α would be a large number when the observed region is extremely homogeneous. If $|\alpha| \to \infty$, then $\Psi^{(1)}(x) \to 0$ and $\Psi^{(2)}(x) \to 0$, consequently $f_1(\infty)$ and $f_2(\infty)$ would be constant as $f_1(\infty) \to (\Psi^{(1)})^{-1}(\widetilde{k_2})$ and $f_2(\infty) \to (\Psi^{(1)})^{-1}(\widetilde{k_3})$. If $f_1(\infty) > f_2(\infty)$, there wouldn't exist any intersection point, and Equation (21) is unsolved.

2.3. Our Proposed Parameter Estimation

In order to obtain the parameters estimation of the G^0 distribution and satisfy the constraints of these parameters, we propose a novel parameter estimation method, which combines the merits both from the MoM and MT parameter estimation. Firstly, we convert Equation (11) into

$$\begin{cases} \alpha = \dfrac{2nE(x^2) - (n+1)E^2(x)}{(n+1)E^2(x) - nE(x^2)} \\ \gamma = -(\alpha+1)E(x) \end{cases}, \quad \alpha < -1, \gamma, n, x > 0 \tag{24}$$

Then, a new Equation is formed by substituting Equation (24) for the second and third expressions of Equation (21)

$$\begin{cases} \log(\gamma/n) + \Psi(n) - \Psi(-\alpha) = \widetilde{k_1} \\ \alpha = \dfrac{2nE(x^2) - (n+1)E^2(x)}{(n+1)E^2(x) - nE(x^2)} \\ \gamma = -(\alpha+1)E(x) \end{cases}, \quad \alpha < -1, \gamma, n, x > 0 \tag{25}$$

Also, we can deduce from Equation (24) that

$$\frac{\gamma}{n} = \frac{E(x^2)E(x)}{nE(x^2) - (n+1)E^2(x)}, \quad \gamma, n, x > 0 \tag{26}$$

Thirdly, the parameter n is obtained by taking Equation (26) and the second expression of Equation (25) into the fist expression of Equation (25).

Finally, the parameter α and γ are obtained subsequently by solving Equation (25).

Our parameter estimation method of the G^0 distribution only requires calculating the 1th-order and 2th-order moments while the MoM based parameter estimation method needs to calculate the 3th-order moment. Additionally, our method avoids the instance of no solution when modeling the extremely homogeneous regions in high resolution SAR images.

For convenience of comparison, the parameter estimation methods of the G^0 distribution mentioned above are summarized in Table 1.

Table 1. The expressions of four methods for parameter estimation of the G^0 distribution mentioned in this paper.

Methods	Expressions
The classical MoM	$k=1/2,\ 1 \begin{cases} \dfrac{\Gamma^2(-\alpha-1/2)\Gamma^2(n+1/2)}{\Gamma(-\alpha-1)\Gamma(n+1)\Gamma(-\alpha)\Gamma(n)} = \dfrac{E^2\left(x^{1/2}\right)}{E(x)} \\ \gamma = n\left(\dfrac{E(x)\Gamma(-\alpha)\Gamma(n)}{\Gamma(-\alpha-1)\Gamma(n+1)}\right)^2 \end{cases}, \ -\alpha,\gamma,n,x>0$
The extended MoM	$k=1,\ 2,\ 3 \begin{cases} E(x) = -\dfrac{\gamma}{\alpha+1} \\ E(x^2) = \dfrac{(n+1)(a+1)}{n(a+2)}E^2(x) \\ E(x^3) = \dfrac{(n+2)(a+1)}{n(a+3)}E^2(x)E(x) \end{cases}, \quad -\alpha,\gamma,n,x>0$
MT	$\begin{cases} \log(\frac{\gamma}{n}) + \Psi(n) - \Psi(-\alpha) = \frac{1}{N}\sum\limits_{i=1}^{N}\log(x_i) = \widetilde{k_1} \\ \Psi^{(1)}(n) + \Psi^{(1)}(-\alpha) = \frac{1}{N}\sum\limits_{i=1}^{N}\left[(\log(x_i) - \widetilde{k_1})^2\right] \\ \Psi^{(2)}(n) - \Psi^{(2)}(-\alpha) = \frac{1}{N}\sum\limits_{i=1}^{N}\left[(\log(x_i) - \widetilde{k_1})^3\right] \end{cases}$
Our proposed	$\begin{cases} \log(\gamma/n) + \Psi(n) - \Psi(-\alpha) = \widetilde{k_1} \\ \alpha = \dfrac{2nE(x^2) - (n+1)E^2(x)}{(n+1)E^2(x) - nE(x^2)} \\ \gamma = -(\alpha+1)E(x) \end{cases}, \quad \alpha < -1,\gamma,n,x>0$

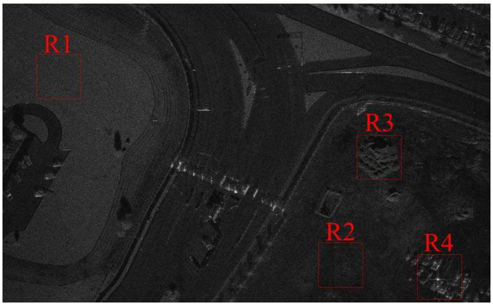

Figure 2. Original SAR image collected by the miniSAR of Sandia National Laboratories, and red rectangles (R1 to R4) indicate the four selected representative regions, which are ground, vegetation, trees and buildings respectively.

3. RESULTS AND DISCUSSION

The proposed parameter estimation method is test in real SAR images. Two SAR images taken from different sensors are used in the experiment. The first one was collected by the Ku-band miniSAR

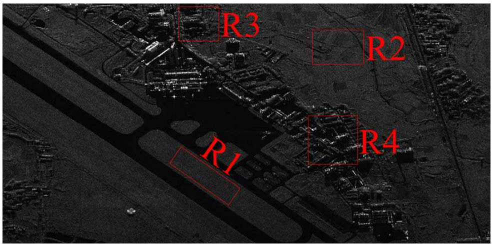

Figure 3. Original SAR image collected by an airborne SAR of China Electronics Technology Group Corporation No. 38 Research Institute, and red rectangles (R1 to R4) indicate the four selected representative regions, which are airdrome ground vegetation, trees and buildings respectively.

Table 2. Parameter estimation results in four regions of Figure 2.

Regions	Methods	Parameters		
		n	α	γ
R1	The classical MoM	4.4	$2.9 * 10^5$	$-6.8 * 10^8$
	The extended MoM	4.4	$1.7 * 10^3$	$-4.0 * 10^6$
	MT	Unsolved	Unsolved	Unsolved
	Our proposed	4.5	-577.5	$1.3 * 10^6$
R2	The classical MoM	3.1	$2.3 * 10^5$	$-1.9 * 10^8$
	The extended MoM	7.3	-8.0	$5.8 * 10^3$
	MT	4.7	-14.2	$1.1 * 10^4$
	Our proposed	5	-11.5	$8.7 * 10^3$
R3	The classical MoM	1.2	$1.2 * 10^5$	$-1.7 * 10^8$
	The extended MoM	1.3	-30.8	$4.2 * 10^4$
	MT	2.2	-3.7	$3.9 * 10^3$
	Our proposed	1.6	-9.4	$1.2 * 10^4$
R4	The classical MoM	0.2	$7.0 * 10^4$	$-1.2 * 10^8$
	The extended MoM	0.4	-3.9	$5.1 * 10^3$
	MT	13.8	-1.6	$1.2 * 10^3$
	Our proposed	2.0	-2.4	$2.4 * 10^3$

of Sandia National Laboratories over the region of Eubank Gated Entrance, KAFB, USA on 19 May 2005. Its size is 2510 × 1638 pixels with a pixel size of about 0.1 m (see Figure 2). The other one was taken by an airborne X-band SAR of China Electronics Technology Group Corporation No. 38 Research Institute over the region of Hefei, Anhui province, China on 6 and 8 November 2005. Its size is 1840 × 907 pixels with a pixel size of about 1 m (see Figure 3). Four representative regions (see red rectangles R1 to R4 in Figure 1 and Figure 2 respectively) are chosen from each SAR image, where R1 is the extremely homogeneous region, R2 is the homogeneous region, R3 is the heterogeneous region, and R4 is the extremely heterogeneous region. All the experiments are run on P(R) dual-core 2.8 GHz CPU, with 2 GB SDRAM, and the software platform is Matlab R2007b.

3.1. Parameter Estimation Experiments

In order to explore the effectiveness of our proposed method, the comparison with other parameter estimation methods is made like the classical MoM [29], our deduced the extended MoM and MT [34]. Table 2 shows the comparative results of these parameter estimation

Table 3. Parameter estimation results in four regions of Figure 3.

Regions	Methods	Parameters		
		n	α	γ
R1	The classical MoM	3.2	$9.3 * 10^4$	$-1.1 * 10^8$
	The extended MoM	4.1	-21.2	$2.3 * 10^4$
	MT	Unsolved	Unsolved	Unsolved
	Our proposed	3.8	-28.3	$3.1 * 10^4$
R2	The classical MoM	2.2	$8.5 * 10^4$	$-1.7 * 10^8$
	The extended MoM	3.5	-9.9	$1.8 * 10^4$
	MT	Unsolved	Unsolved	Unsolved
	Our proposed	2.6	-22.8	$4.4 * 10^4$
R3	The classical MoM	0.3	$2.7 * 10^4$	$-4.7 * 10^7$
	The extended MoM	0.4	-5.7	$8.1 * 10^3$
	MT	1.4	-1.4	875.9
	Our proposed	0.8	-3.1	$3.7 * 10^3$
R4	The classical MoM	0.1	$4.0 * 10^4$	$-5.8 * 10^7$
	The extended MoM	0.1	-7.9	$9.9 * 10^3$
	MT	2.5	-0.9	211.8
	Our proposed	0.6	-2.3	$1.9 * 10^3$

Table 4. Time consuming of the four mentioned methods in four regions of Figure 2.

Region		R1	R2	R3	R4
Size (pixels)		235 × 235	235 × 235	235 × 235	235 × 235
Time consuming (s)	The classical MoM	0.38	0.36	0.37	0.39
	The extended MoM	0.55	0.62	0.67	0.68
	MT	263	387	325	3.09
	Our proposed	0.01	0.01	0.02	0.04

algorithms of four representative regions in Figure 2, and Table 3 shows the comparative results of these parameter estimation algorithms of four representative regions in Figure 3.

According to Equation (10), the estimated parameters should meet the requirement that α is negative and γ, n, x are positive. However, it can be seen that the parameters like α and γ obtained by the classical MoM exceed the range of the requirement of Equation (10) both in Table 2 and Table 3. The parameters like α and γ obtained by the extended MoM seldom exceed the range of definition except in the region of R1 in Table 2.

The key-point of MT based parameter estimation is calculating the intersection point of the inverse digamma function $f_1(x)$ and $f_2(x)$. When modeling the extremely homogeneous regions, MT cannot arrive at a solution, and sometime the same thing is met when modeling the homogeneous region. To deeply evaluate the MT based method, we draw the curves of $f_1(x)$ and $f_2(x)$. Figure 4 shows the inverse digamma function curves $f_1(x)$ and $f_2(x)$ in four regions of Figure 2, and Figure 5 shows the inverse digamma function curves $f_1(x)$ and $f_2(x)$ in four regions of Figure 3. It can be seen that the two curves $f_1(x)$ and$f_2(x)$ don't intersect in Figure 4(a), Figure 5(a) and Figure 5(b). It means that no solution is arrived at, which is consistent with the MT parameters estimation results of R1 in Table 2, and R1 and R2 in Table 3.

Compared with the above three methods, the parameters obtained by our proposed method are met with the requirement of Equation (10) both in Table 2 and Table 3. According to literature [16] stated, the degree of heterogeneity can be measured with the estimated value of α, i.e., if estimation is performed over two areas α_1 and α_2 are the estimated parameters, then $\alpha_1 > \alpha_2$ suggests that the first area is more heterogeneous than the second one. Figure 6 shows parameter α estimated by our method over a variety of areas (ground vegetation, trees and buildings) in two high resolution SAR images Figure 2 and

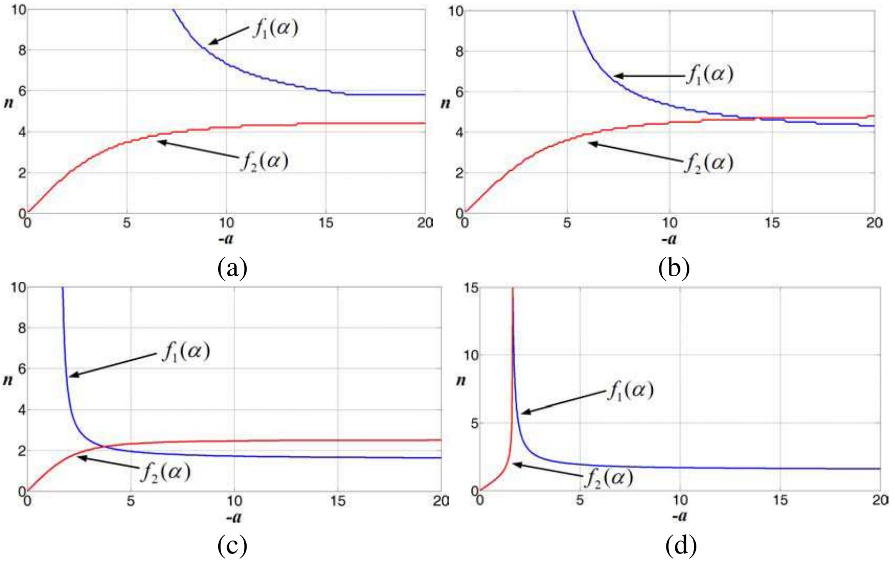

(a) (b) (c) (d)

Figure 4. MT based α and n estimation method by calculating the intersection point of $f_1(x)$ and $f_2(x)$ in four regions (R1 to R4) of Figure 2, the blue curve represents $f_1(\alpha)$ and the red curve represents $f_2(\alpha)$. (a) R1. (b) R2. (c) R3. (d) R4.

Figure 3. It can be seen that parameter α increases with degree of heterogeneity. The results of Figure 6 are consistent with the statement of literature [16].

Table 4 and Table 5 show the time consumed in estimating parameters in these eight regions of Figure 2 and Figure 3. The MT costs the longest time owing to the time-consuming computation of inverse digamma functions. The time-consuming of the classical MoM and the extended MoM is medial, and the extended MoM costs more time than the classical MoM because of higher order moments calculation. Our proposed is the fastest one among these four parameter estimation methods due to no higher moments calculation and inverse digamma function computation.

3.2. Fitting Precision Experiments

In order to evaluate the performance of our algorithm thoroughly, we adopt three well-known parameters like the KL distance [36], KS test [37] and MSE [35] as goodness of fit measurements.

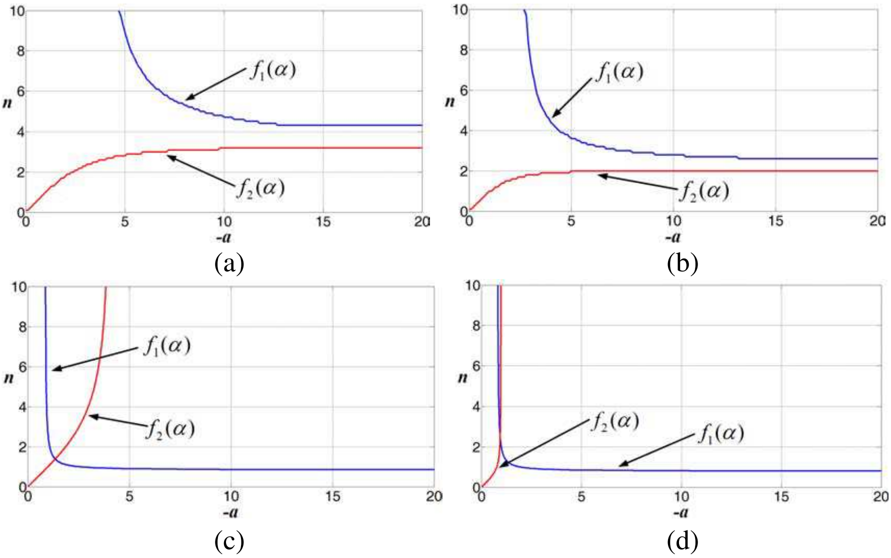

(a) (b)

(c) (d)

Figure 5. MT based α and n estimation method by calculating the intersection point of $f_1(x)$ and $f_2(x)$ in four regions (R1 to R4) of Figure 3, the blue curve represents $f_1(\alpha)$ and the red curve represents $f_2(\alpha)$. (a) R1. (b) R2. (c) R3. (d) R4.

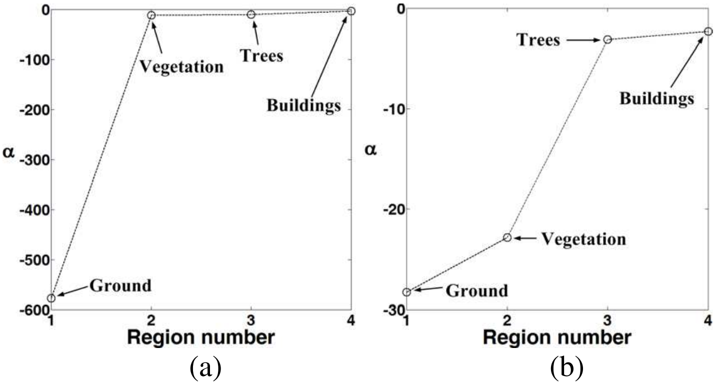

(a) (b)

Figure 6. Parameter α estimated by our method over four areas (ground vegetation, trees and buildings) in two high resolution SAR images. (a) Four areas in Figure 2. (b) Four areas in Figure 3.

3.2.1. KL Distance Measurement

Given the theoretical PDF $p(w)$ and the estimated PDF $q(w)$, the traditional KL distance between these two densities p and q is expressed

Table 5. Time consuming of the four mentioned methods in four regions of Figure 3.

Region		R1	R2	R3	R4
Size (pixels)		78 × 282	133 × 200	133 × 157	192 × 192
Time consuming (s)	The classical MoM	0.12	0.22	0.15	0.24
	The extended MoM	0.41	0.45	0.42	0.48
	MT	1.74	2.52	2.38	2.22
	Our method	0.01	0.01	0.01	0.02

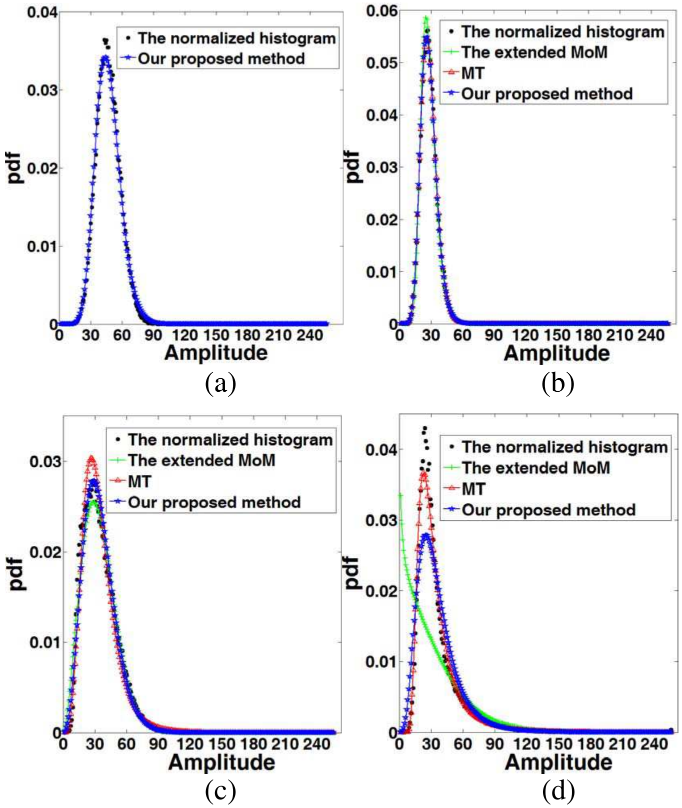

(a) (b)

(c) (d)

Figure 7. Fitting results of four regions histogram in Figure 2. (a) R1 the extremely homogeneous region. (b) R2 the homogeneous region. (c) R3 the heterogeneous region. (d) R4 the extremely heterogeneous region.

as

$$D(q\|p) = \int q(w) \log_2 \left(\frac{q(w)}{p(w)} \right) dw \tag{27}$$

Usually, the calculation of $D(q\|p)$ is given by approximate calculation:

$$D(q\|p) = \sum q(w)\Delta w \log_2 \left(\frac{q(w)\Delta w}{p(w)\Delta w} \right) = \sum Q(w) \log_2 \left(\frac{Q(w)}{P(w)} \right) \tag{28}$$

where $P(w)$ and $Q(w)$ are the values of probability. Because $D(q\|p)$ is asymmetrical, the KL distance is customarily expressed as a symmetrical form

$$D_{kl} = D(q\|p) + D(p\|q) \tag{29}$$

The KL distance reflects the similarity of the theoretical and estimated densities. When the estimated PDF equals the theoretical

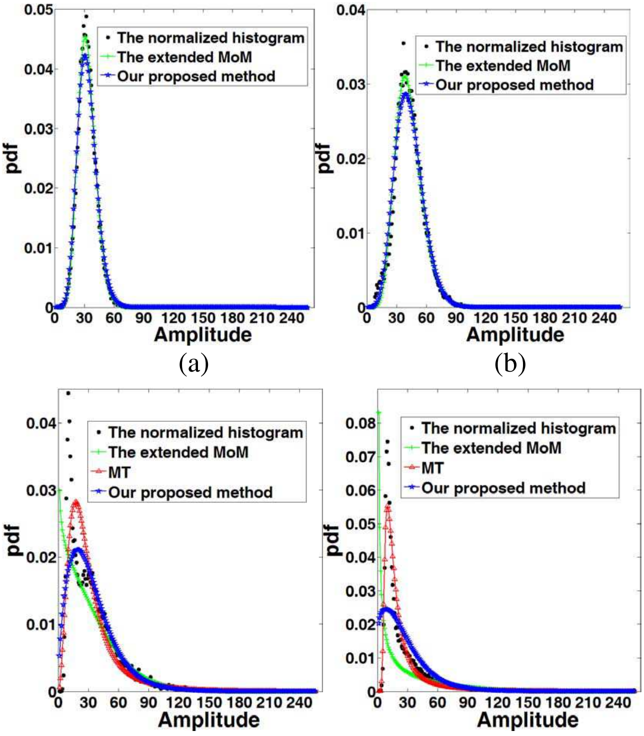

(a) (b)

(c) (d)

Figure 8. Fitting results of four regions histogram in Figure 3. (a) R1 the extremely homogeneous region. (b) R2 the homogeneous region. (c) R3 the heterogeneous region. (d) R4 the extremely heterogeneous region.

PDF, D_{kl} is zero. Otherwise, it is positive. The smaller the value of the KL distance is obtained the higher similarity they have.

3.2.2. KS Test

The KS test is based on the empirical cumulative distribution function (CDF) of the observed data. Given N observations $R_1, R_2, \ldots, R_N$ with continuous distributions, statistical goodness-of-fit is used to choose between hypothesis H_0, an assertion that the data obeys distribution q; and an alternative hypothesis H_1, an assertion that the data does not obey distribution q. The empirical CDF $\widehat{P_R}(w)$ is a piecewise constant function

$$\widehat{P_R}(w) = \begin{cases} 0, & w \to \infty \\ \frac{k}{N}, & R_k < w \le R_{k+1},\ k \le N-1 \\ 1, & w > R_N \end{cases} \tag{30}$$

The KS test D_{ks} is defined as the supremum of the magnitude difference between the empirical CDF $\widehat{P_R}(w)$ and the cumulative distribution under hypothesis H_0, $Q_R(w)$

$$D_{ks} = \sup_w \left| \widehat{P_R}(w) - Q_R(w) \right| \tag{31}$$

The KS test reflects the maximal deviation between the actual CDF and hypothetical CDF. The smaller the value of the KS test is obtained the higher goodness-of-fit they have. It is complementary for the KL distance measurement.

3.2.3. MSE Measurement

Given N discrete samples $r_1, r_2, \ldots, r_N$ with the theoretical PDF $p(w)$ and the estimated PDF $q(w)$, the MSE measurement is expressed as

$$D_{mse} = \frac{1}{N} \sum_{k=1}^{N} \|p(r_k) - q(r_k)\|^2 \tag{32}$$

where $\|\cdot\|$ denotes the Euclidean norm and the estimated PDF $q(w)$ can be deduced from the histogram of the sample values. The MSE measurement reflects the mean deviation between theoretical PDF and the estimated PDF. The smaller the value of the MSE Measurement is the higher goodness-of-fit they have.

Figure 7 and Figure 8 show the fitting results of histogram in eight regions of Figure 2 and Figure 3 by using the classical MoM, the extended MoM, MT and our proposed method. In Figure 7 and Figure 8, the horizontal axis represents the amplitude of pixel, and the

Table 6. The quantity comparison of fitting results of the histogram in Figure 2 based on these four parameter estimation methods, where D_{kl} denotes the KL distance, D_{ks} denotes the KS test, and D_{mse} denotes the MSE measurement.

Regions	Methods	Measurements		
		D_{kl}	D_{ks}	D_{mse}
R1	The classical MoM	Unsolved	Unsolved	Unsolved
	The extended MoM	Unsolved	Unsolved	Unsolved
	MT	Unsolved	Unsolved	Unsolved
	Our proposed	0.02	0.02	$1.7 * 10^{-9}$
R2	The classical MoM	Unsolved	Unsolved	Unsolved
	The extended MoM	0.02	0.02	$3.1 * 10^{-9}$
	MT	0.00	0.00	$4.5 * 10^{-10}$
	Our proposed	0.00	0.01	$7.1 * 10^{-10}$
R3	The classical MoM	Unsolved	Unsolved	Unsolved
	The extended MoM	0.12	0.03	$5.8 * 10^{-9}$
	MT	0.05	0.03	$6.4 * 10^{-9}$
	Our proposed	0.06	0.02	$5.4 * 10^{-9}$
R4	The classical MoM	Unsolved	Unsolved	Unsolved
	The extended MoM	1.3	0.3	$2.6 * 10^{-7}$
	MT	0.03	0.02	$6.0 * 10^{-9}$
	Our proposed	0.23	0.08	$3.7 * 10^{-8}$

vertical axis represents the PDF. Based on Equations (29), (31) and (32), the KL distance, the KS test, and the MSE measurement of the fitting results shown in Figure 7 are compared in Table 6, and these shown in Figure 8 are compared in Table 7. In Figure 7(a), it can be seen that only the G^0 distribution density function solved by our proposed method can fit the normalized histogram of the extremely homogeneous SAR regions. The G^0 distribution density function solved by the extended MoM based method can model most of regions, but the fitting precisions are relatively low. The G^0 distribution density function solved by the MT based method agrees well with the histogram of the heterogeneous and extremely heterogeneous regions in Figure 7(d) and Figure 8(d). Because the parameters estimated by the classical MoM method exceed the range of the requirement of Equation (10), the G^0 distribution density function of these eight regions has no solution. The quantity evaluation results of goodness-of-fit in Table 6 and Table 7 agree well with the fitness of the normalized histogram of these eight different degrees of heterogeneity regions in

Table 7. The fitting results of the histogram in Figure 3 based on these four parameter estimation methods, where D_{kl} denotes the KL distance, D_{ks} denotes the KS test, and D_{mse} denotes the MSE.

Regions	Methods	Measurements		
		D_{kl}	D_{ks}	D_{mse}
R1	The classical MoM	Unsolved	Unsolved	Unsolved
	The extended MoM	0.01	0.01	$3.9 * 10^{-9}$
	MT	Unsolved	Unsolved	Unsolved
	Our proposed	0.01	0.01	$4.7 * 10^{-9}$
R2	The classical MoM	Unsolved	Unsolved	Unsolved
	The extended MoM	0.07	0.02	$8.0 * 10^{-9}$
	MT	Unsolved	Unsolved	Unsolved
	Our proposed	0.05	0.03	$1.3 * 10^{-8}$
R3	The classical MoM	Unsolved	Unsolved	Unsolved
	The extended MoM	0.87	0.15	$2.7 * 10^{-7}$
	MT	0.23	0.07	$1.3 * 10^{-7}$
	Our proposed	0.34	0.07	$1.4 * 10^{-7}$
R4	The classical MoM	Unsolved	Unsolved	Unsolved
	The extended MoM	2.72	0.33	$7.9 * 10^{-7}$
	MT	0.10	0.05	$5.0 * 10^{-8}$
	Our proposed	1.07	0.16	$3.4 * 10^{-7}$

Figure 7 and Figure 8.

From these experimental analyses, some conclusions can be drawn:

(1) Our parameter estimation scheme of the G^0 distribution has a wider modeling ability and lower computation time than the other three methods, but the fitting precision of which is lower than the MT based method when modeling the heterogeneous and extremely heterogeneous regions.

(2) The classical MoM based method can not model any regions of these two high resolution SAR images.

(3) The extended MoM based method is able to model most regions of these two high resolution SAR images, but the goodness-of-fit of which is the worst among these four methods.

(4) The MT based method has a higher fitting precision than the others when modeling the heterogeneous and extremely heterogeneous regions, but the calculation time of which is the longest among these four methods. Furthermore, it can not model the extremely homogeneous regions in high resolution SAR images.

4. CONCLUSIONS

Aiming at having a wider modeling ability in high resolution SAR images, this paper has proposed an improved parameter estimation scheme of the G^0 distribution, which combines the merits from the classical moment estimation and the mellin transform. Results show that our proposed method is suitable for modeling multilook clutter with widely various degrees of homogeneity, and has lower computation time than the other mentioned methods.

The next step is to increase the fitting precision when modeling the heterogeneous and extremely heterogeneous regions. It would also be interesting to use the proposed method for objects classification in high resolution SAR images.

ACKNOWLEDGMENT

The authors would like to thank all the reviewers for their valuable suggestions and comments. This paper is supported by the National Natural Science Foundation of China (No. 41171316).

REFERENCES

1. Koo, V. C., Y. K. Chan, V. Gobi, M. Y. Chua, C. H. Lim, C. S. Lim, C. C. Thum, T. S. Lim, Z. Bin Ahmad, K. A. Mahmood, M. H. Bin Shahid, C. Y. Ang, W. Q. Tan, P. N. Tan, K. S. Yee, W. G. Cheaw, H. S. Boey, A. L. Choo, and B. C. Sew, "A new unmanned aerial vehicle synthetic aperture radar for environmental monitoring," *Progress In Electromagnetics Research*, Vol. 122, 245–268, 2012.
2. Chan, Y. K. and V. C. Koo, "An introduction to synthetic aperture radar (SAR)," *Progress In Electromagnetics Research B*, Vol. 2, 27–60, 2008.
3. Mohammadpoor, M., R. S. A. Raja Abdullah, A. Ismail, and A. F. Abas, "A circular synthetic aperture radar for on-the-ground object detection," *Progress In Electromagnetics Research*, Vol. 122, 269–292, 2012.
4. Tian, B., D.-Y. Zhu, and Z.-D. Zhu, "A novel moving target detection approach for dual-channel SAR system," *Progress In Electromagnetics Research*, Vol. 115, 191–206, 2011.
5. Park, S. H., J. H. Lee, and K. T. Kim, "Performance analysis of the scenario-based construction method for real target ISAR

recognition," *Progress In Electromagnetics Research*, Vol. 128, 137–151, 2012.

6. Chang, Y.-L., C.-Y. Chiang, and K.-S. Chen, "SAR image simulation with application to target recognition," *Progress In Electromagnetics Research*, Vol. 119, 35–57, 2011.
7. Park, J.-I. and K.-T. Kim, "A comparative study on ISAR imaging algorithms for radar target identification," *Progress In Electromagnetics Research*, Vol. 108, 155–175, 2010.
8. Zhao, Y. W., M. Zhang, X. P. Geng, and P. Zhou, "A comprehensive facet model for bistatic SAR imagery of dynamic ocean scene," *Progress In Electromagnetics Research*, Vol. 123, 427–445, 2012.
9. Albert, M. D., Y. J. Lee, H. T. Ewe, and H. T. Chuah, "Multilayer model formulation and analysis of radar backscattering from sea ice," *Progress In Electromagnetics Research*, Vol. 128, 267–290, 2012.
10. Dusséaux, R., E. Vannier, O. Taconet, and G. Granet, "Study of backscatter signature for seedbed surface evolution under rainfall-influence of radar precision," *Progress In Electromagnetics Research*, Vol. 125, 415–437, 2012.
11. Feng, L., H. Xu, C.-S. Li, S. Li, and H. Gao, "A novel estimation approach of dynamic and coupling baseline for distributed satellite SAR," *Progress In Electromagnetics Research*, Vol. 123, 467–484, 2012.
12. Bausssard, A., M. Rochdi, and A. Khenchaf, "Po/mec-based scattering model for complex objects on a sea surface," *Progress In Electromagnetics Research*, Vol. 111, 229–251, 2011.
13. Jin, Y. Q., "Polarimetric scattering modeling and information retrieval of SAR remote sensing — A review of FDU work," *Progress In Electromagnetics Research*, Vol. 104, 333–384, 2010.
14. Liu, D., Y. Du, G. Sun, W.-Z. Yan, and B.-I. Wu, "Analysis of InSAR sensitivity to forest structure based on radar scattering model," *Progress In Electromagnetics Research*, Vol. 84, 149–171, 2008.
15. Du, Y., Y. Luo, W.-Z. Yan, and J. A. Kong, "An electromagnetic scattering model for soybean canopy," *Progress In Electromagnetics Research*, Vol. 79, 209–223, 2008.
16. Frery, A. C., H. J., Muller, C. D. Costa, C. D. C. F. Yanasse, and S. J. S. Sant' Anna, "A model for extremely heterogeneous clutter," *IEEE Transactions on Geoscience and Remote Sensing*, Vol. 35, No. 3, 648–659, 1997.

17. Gao, G., "Statistical modeling of SAR images: A survey," *Sensors*, Vol. 10, 775–795, 2010.
18. Bruzzone, J., M. Marconcini, U. Wegmuller, and A. Wiesmann, "An advanced system for the automatic classification of multitemporal SAR images," *IEEE Transactions on Geoscience and Remote Sensing*, Vol. 42, No. 6, 1321–1334, 2004.
19. Luo, M. and K.-M. Huang, "Prediction of the electromagnetic field in metallic enclosures using artificial neural networks," *Progress In Electromagnetics Research*, Vol. 116, 171–184, 2011.
20. O'Halloran, M., B. McGinley, R. C. Conceicao, F. Morgan, E. Jones, and M. Glavin, "Spiking neural networks for breast cancer classification in a dielectrically heterogeneous breast," *Progress In Electromagnetics Research*, Vol. 113, 413–428, 2011.
21. Zaharis, Z. D., K. A. Gotsis, and J. N. Sahalos, "Comparative study of neural network training applied to adaptive beamforming of antenna arrays," *Progress In Electromagnetics Research B*, Vol. 126, 269–283, 2012.
22. Zaharis, Z. D., K. A. Gotsis, and J. N. Sahalos, "Adaptive beamforming with low Side lobe level using neural networks trained by mutated boolean PSO," *Progress In Electromagnetics Research*, Vol. 127, 139–154, 2012.
23. Mantero, P., "Partially supervised classification of remote sensing images using SVM-based probability density estimation," *IEEE Transactions on Geoscience and Remote Sensing*, Vol. 43, No. 3, 559–570, 2005.
24. Tan, C.-P., J.-Y. Koay, K.-S. Lim, H.-T. Ewe, and H.-T. Chuah, "Classification of multi-temporal SAR images for rice crops using combined entropy decomposition and support vector machine technique," *Progress In Electromagnetics Research*, Vol. 71, 19–39, 2007.
25. Gao, G., "A parzen-window-kernel-based CFAR algorithm for ship detection in SAR images," *IEEE Geoscience and Remote Sensing Letters*, Vol. 8, No. 3, 557–561, 2011.
26. Oliver, C. J., *Understanding Synthetic Aperture Radar Images*, Artech House, Boston, London, USA, UK, 1998.
27. Moser, G. J., S. Zerubia, and B. Serpico, "Dictionary-based stochastic expectation — Maximization for SAR amplitude probability density function estimation," *IEEE Transactions on Geoscience and Remote Sensing*, Vol. 44, No. 1, 188–200, 2006.
28. Joughin, I. R., "Maximum likelihood estimation of K distribution parameters for SAR data," *IEEE Transactions on Geoscience and*

Remote Sensing, Vol. 31, No. 5, 989–999, 1993.

29. Freitas, C. C., A. C. Frery, and A. H. Correia, "The polarimetric G distribution for SAR data," *Environmetries*, Vol. 16, No. 1, 13–31, 2005.
30. Allende, H., A. C. Frery, J. Galbiati, and L. Pizarro, "M-estimators with asymmetric influence functions: The G^0 distribution case," *Journal of Statistical Computation and Simulation*, Vol. 76, No. 11, 941–956, 2006.
31. Liu, Z. L. and J. Yang, "Analysis of electromagnetic scattering with higher-order moment method and NURBS model," *Progress In Electromagnetics Research*, Vol. 96, 83–100, 2009.
32. Hatamzadeh-Varmazyar, S. H., M. Naser-Moghadasi, and Z. Masouri, "A moment method simulation of electromagnetic scattering from conducting bodies," *Progress In Electromagnetics Research*, Vol. 81, 99–119, 2008.
33. Wang, S., X. Guan, D. W. Wang, X. Ma, and Y. Su, "Electromagnetic scattering by mixed conducting/dielectric objects using higher-order MoM," *Progress In Electromagnetics Research*, Vol. 66, 51–63, 2006.
34. Shi, G. T., G. Gao, X. G. Zhou, G. Y. Kuang, and Y. M. Jiang, "Parameter estimation of G^0 distribution based on Mellin transform," *Progress in Natural Science*, Vol. 19, No. 6, 677–690, 2009.
35. Tison, C., J. M. Nicolas, F. Tupin, and H. Maître, "A new statistical model for Markovian classification of urban areas in high-resolution SAR images," *IEEE Transactions on Geoscience and Remote Sensing*, Vol. 42, No. 10, 2046–2057, 2004.
36. Cover, T. M. and J. A. Thomas, *Elements of Information Theory*, Wiley Interscience, New York, 1991.
37. DeVore, M. D. and J. A. O'Sullivan, "Quantitative statistical assessment of conditional models for synthetic aperture radar," *IEEE Transactions on Image Processing*, Vol. 13, No. 2, 113–125, 2004.
38. Yueh, S. H., J. A. Kong, J. K. Jao, R. T. Shin, H. A. Zebker, T. Le Toan, and H. Öttl, "K-distribution and polarimetric terrain radar clutter," *Progress In Electromagnetics Research*, Vol. 3, 237–275, 1990.